NRIAG Journal of Astronomy and Geophysics xxx (2017) xxx–xxx

Contents lists available at ScienceDirect

NRIAG Journal of Astronomy and Geophysics

journal homepage: www.elsevier.com/locate/nrjag

Full length article

# Investigating the use of the dual-polarized and large incident angle of SAR data for mapping the fluvial and aeolian deposits

Ahmed Gaber [a,*], Bassam A. Amarah [b], Mohamed Abdelfattah [a], Sarah Ali [a]

[a] Geology Department, Faculty of Science, Port-Said University, Egypt
[b] Geology & Geophysics Department, College of Science, King Saud University, Saudi Arabia

ARTICLE INFO

*Article history:*
Received 5 September 2017
Revised 17 October 2017
Accepted 17 October 2017
Available online xxxx

*Keywords:*
Dual-polarized SAR data
Mapping fluvial deposits
Incident angle of SAR signals
Imaging near-surface features
Aeolian sand cover

ABSTRACT

Mapping the spatial distributions of the fluvial deposits in terms of particles size as well as imaging the near-surface features along the non-vegetated aeolian sand-sheets, provides valuable geological information. Thus this work aims at investigating the contribution of the dual-polarization SAR data in classifying and mapping the surface sediments as well as investigating the effect of the radar incident-angle on improving the images of the hidden features under the desert sand cover. For mapping the fluvial deposits, the covariance matrix ($[C_2]$) using four dual-polarized ALOS/PALSAR-1 scenes cover the Wadi El Matulla, East Qena, Egypt were generated. This $[C_2]$ matrix was used to generate a supervised classification map with three main classes (gravel, gravel/sand and sand). The polarimetric scattering response, spectral reflectance and temperatures brightness of these 3 classes were extracted. However for the aeolian deposits investigation, two Radarsat-1 and three full-polarimetric ALOS/PALSAR-1 images, which cover the northwestern sandy part of Sinai, Egypt were calibrated, filtered, geocoded and ingested in a GIS database to image the near-surface features. The fluvial mapping results show that the values of the radar backscattered coefficient ($\boldsymbol{\sigma}^{\circ}$) and the degree of randomness of the obtained three classes are increasing respectively by increasing their grain size. Moreover, the large incident angle ($\theta_i = 39.7$) of the Radarsat-1 image has revealed a meandering buried stream under the sand sheet of the northwestern part of Sinai. Such buried stream does not appear in the other optical, SRTM and SAR dataset. The main reason is the enhanced contrast between the low backscattered return from the revealed meandering stream and the surroundings as a result of the increased backscattering intensity, which is related to the relatively large incident angle along the undulated surface of the study area. All archaeological observations support the existence of paleo-fresh water lagoon at the northwestern corner of the study area, which might have been the discharge lagoon of the revealed hidden stream.



## 1. Background

Generating accurate maps for the surface and near-surface sediments along the non-vegetated areas covered by fluvial and aeolian interchange processes in terms of grains sizes, hidden features can reveal valuable geological information (Gaber et al., 2015). Usually, such maps are rarely available although they may provide useful information about the aeolian and fluvial interplay, and thus reveal clearly the depositional history of these sediments. Meanwhile, the polarimetric studies of Synthetic Aperture Radar (SAR) data became an important research topic since dual and full polarimetric SAR data have become routinely available. Accordingly, the use of polarimetric information of SAR data in mapping the different surface land covers has been explored by many researchers (Van Zyl et al., 1987; Van Zyl, 1989; Papathanassiou and Buchroithner, 1993; Cloude and Pottier, 1997; Lee et al., 1999; Zhang et al., 2011; Gaber et al., 2015). Several polarimetric decomposition and classification theorems, which investigate the radar backscattering mechanisms, were introduced (Cloude and Pottier, 1996; Freeman and Durden, 1998; Yang et al., 1998; Yamaguchi et al., 2005).

* Corresponding author.
*E-mail address:* ahmedgaber_881@hotmail.com (A. Gaber).

Peer review under responsibility of National Research Institute of Astronomy and Geophysics.

Production and hosting by Elsevier

https://doi.org/10.1016/j.nrjag.2017.10.005
2090-9977/

Please cite this article in press as: Gaber, A., et al. Investigating the use of the dual-polarized and large incident angle of SAR data for mapping the fluvial and aeolian deposits. NRIAG Journal of Astronomy and Geophysics (2017), https://doi.org/10.1016/j.nrjag.2017.10.005

Moreover, the polarization signature, which investigates the power, ellipticity degree ($\chi$) and orientation angle ($\psi$) of the returned SAR signals from each land cover has been also used for accurately discriminating between these land covers (Rignot et al., 1992; Chen et al., 1996; Cloude and Pottier, 1997; Lee et al., 1999; Ferro-Famil et al.; 2001; Barnes and Burki, 2006; Cameron and Rais, 2006; Alberga, 2007; Gaber et al., 2015). Most of previous works that have been performed for mapping the surficial sediments in desert areas were acquired using the full-polarimetric SAR information (HH, HV, VH and VV) and very limited works have discovered the contribution of the dual-polarization (HH and HV) data to achieve the same objectives in mapping the surficial sediments based on their scattering response.

On the other hand, the penetration capability of SAR sensors and the intensity of the backscattering returned waves depend on the following: (1) characteristics of transmitted signals; wavelength, polarization, incidence angle and look angle and (2) characteristics of the imaged targets; surface roughness and dielectric constant ($\varepsilon$). The radar waves that penetrating the earth's materials are subjected to attenuation and in case of significant attenuation, the waves will be damped rapidly until reaching the skin depth. The depth of penetration is defined as the depth within a medium at which the power of a propagating wave is equal to $e^{-1}$ of its power at the medium's surface (Ulaby et al., 1982). The depth of penetration ($\delta p$) is a function of the scattering and absorption losses within a medium, and can be calculated by the following equation (Ulaby et al., 1982):

$$\delta p = \frac{\lambda}{4\pi} \frac{1}{\sqrt{\left\{\left[1+\left(\frac{\varepsilon''}{\varepsilon'}\right)^2\right]^{\frac{1}{2}}-1\right\}*\frac{\varepsilon'}{2}}} \quad (1)$$

where $\lambda$ is the wavelength in free space and $\varepsilon'$ and $\varepsilon''$ are the real part and imaginary part of the dielectric permittivity of the medium. The depth of penetration ($\delta p$) represents the maximum depth within a medium that can contribute to the backscattering coefficient. In a medium with good conductivity, the depth of penetration could be expressed by the following equation (Ghasemi et al., 2016):

$$\delta p = \frac{1}{\sqrt{\pi f \mu \sigma}} \quad (2)$$

where $\delta p$, f, $\mu$ and $\sigma$ represent the depth of penetration, frequency, medium permeability, and medium conductivity, respectively, and all are in metric units. Since $\delta p$ is inversely proportional to the square root of the frequency (wavelength), hence it reduces by increasing the frequency (shorter wavelength). Evidently because of high value of $\delta p$, propagation of radar waves is limited and rather difficult in materials with high dielectric constant. In addition, Lusch (1999) stated that the penetration depth ($\delta p$) is directly related to the wavelength (longer wavelength penetrate more), inversely related to the dielectric constant of the medium and inversely related to the incidence angle ($\tan\theta i$), which means the lower incidence angles the more depths would be penetrated by radar waves and expressed by the following equation:

$$\delta p = \frac{\lambda}{\pi \varepsilon \tan\theta} \quad (3)$$

where $\delta p$, $\lambda$, $\varepsilon$, and ($\theta i$) represent the depth of penetration, wavelength, dielectric constant of the medium, and incidence angle, respectively. Furthermore, it has been proven that there is a good relationship between the local incident angle and the intensity of the radar backscattered returned wave from the targets and it is a function of its structural and dielectric properties (O'Grady et al., 2013). Mouginis (2017) stated that, the smooth surfaces act like a mirror when the incident angle ($\theta_i$) is small. The opposite is true for rough surfaces, which means for the rough surfaces the backscattered radar return will be increased by increasing the incident angle (Fig. 1). Consequently, this is enhancing the contrast between the low backscattered return from targets and the relatively high backscattered radar return from the surroundings.

The investigators who used the space-borne SAR data to image and map the near-surface features, which are covered by the wind-blown dry sand of Eastern Sahara, they imaged details of hidden drainage patterns, paleo-lakes as well as faults that underlie the sand sheets (McCauley et al., 1982; Elachi et al., 1984; Schaber et al., 1986; Farr et al., 1986; Schaber et al., 1987; Abdelsalam et al., 2000; Robinson et al., 2000; Paillou et al., 2003, 2006, 2009, 2010; El-Baz et al., 2007; Ghoneim et al., 2007; Gaber et al., 2015; Paillou, 2017). All of those investigators agreed that, in very dry soils with low electrical loss materials such as desert sand, SAR is able to probe the subsurface down to several meters (Elachi et al., 1984; Farr et al., 1986; Paillou, 2017). However few of those investigators have talked in details about the contribution of the radar incident-angle ($\theta_i$) in improving the penetration capability and the intensity of the backscattered radar returns with a clear example.

Thus this work aims at; (1) investigating the contribution of the dual-polarization (HH and HV) SAR data to classify and map the surface sediments in terms of grain sizes in East Qena, Egypt and (2) introducing a real world example of the relationship between the radar incident-angle and the penetration depth with the amount of radar backscattered returns along a non-vegetated desert area covered by dry sand at the Northwestern part of Sinai Peninsula, Egypt.

## 2. Descriptions of the selected study areas

Two different case studies were selected to carry out this research. The first case study is covered by fluvial deposits, while the second one is covered by aeolian sand. The detailed descriptions of these sites are in the next section.

### 2.1. Wadi El Matulla, East Qena (1st case study)

In this case study, the selected area extends from the Red Sea Mountains to the Nile Valley between longitude 32°48′E and

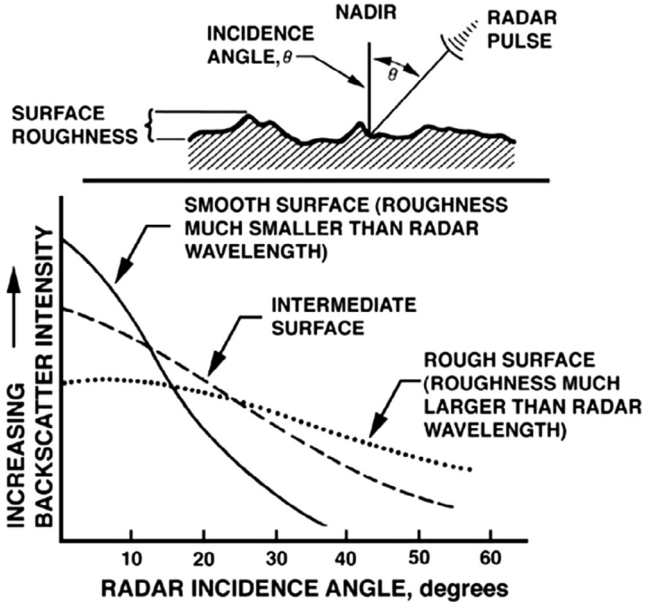


**Fig. 1.** The relationship between the incident angle ($\theta_i$) and the radar backscattered intensity (Mouginis, 2017).

Please cite this article in press as: Gaber, A., et al. Investigating the use of the dual-polarized and large incident angle of SAR data for mapping the fluvial and aeolian deposits. NRIAG Journal of Astronomy and Geophysics (2017), https://doi.org/10.1016/j.nrjag.2017.10.005

34°20′E and latitude 25°25′N and 26°20′N (Fig. 2). It covers approximately an area of 7500 km$^2$, which is a vast valley extends westward to about 130 km from its eastern upstream and named Wadi El Matulla. It has an E-W trend and gently dips to the west until it joins the Nile River at Qift City. Its major tributaries including Wadi El-Hammamat, Wadi Zaidun, Wadi El-Mishash, and Wadi El-Muweih. It is covered by the basement complex on the eastern side and constitutes the upstream of Wadi El Matulla (EGSM, 1987). However, the western part is represented by Cretaceous/Tertiary sedimentary rocks unconformable with the underlain basement complex. Finally, the wadi deposits (Pliocene-Pleistocene), which is our interest; cover the lowest relief parts along the study area (Fig. 2).

### 2.2. Northwestern Sinai (2nd case study)

The northwestern part of Sinai Peninsula comprises of five distinctive geomorphologic units; the coastal area, El-Bardawil lagoon, aeolian sand, sand dunes and salt marshes and sabkhas (Al Hussein et al., 2012). It is entirely covered by Quaternary sediments of aeolian and alluvial origin, which show a variation in their texture and composition ranging from unconsolidated sands to silt and clay (Fig. 3). The sand dune deposits are deflected and diverted from northwest to southeast direction due to the local winds regime. The sabkhas are situated in low-relief areas between hummocky surfaces and sand dunes as a result of high evaporation for the shallow groundwater and occasional rainfall water. The study area has a slightly undulated surface of sand dunes. In this case study, different radar images were used to investigate the relationship between the incident angle and the intensity of the

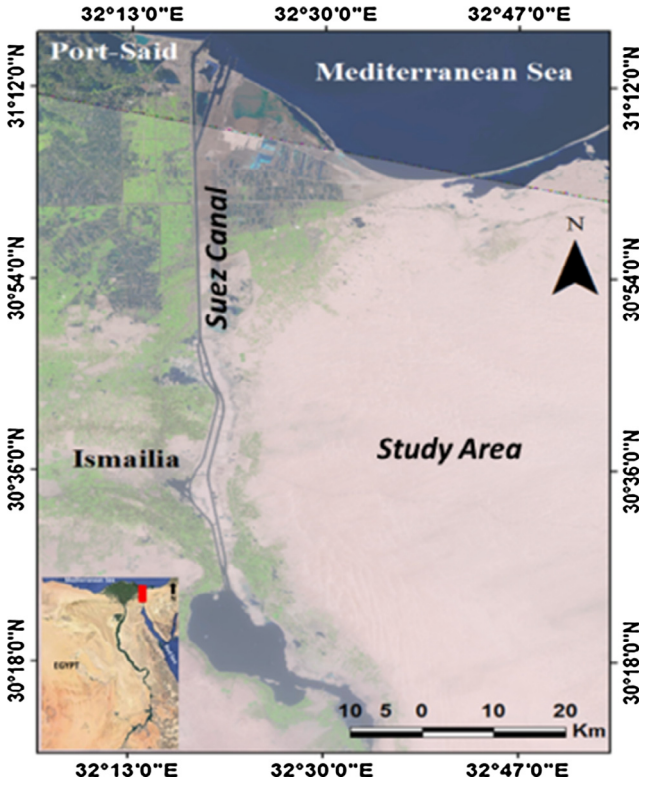


**Fig. 3.** Optical satellite image showing the feature-less sand sheets along the Northwestern part of Sinai.

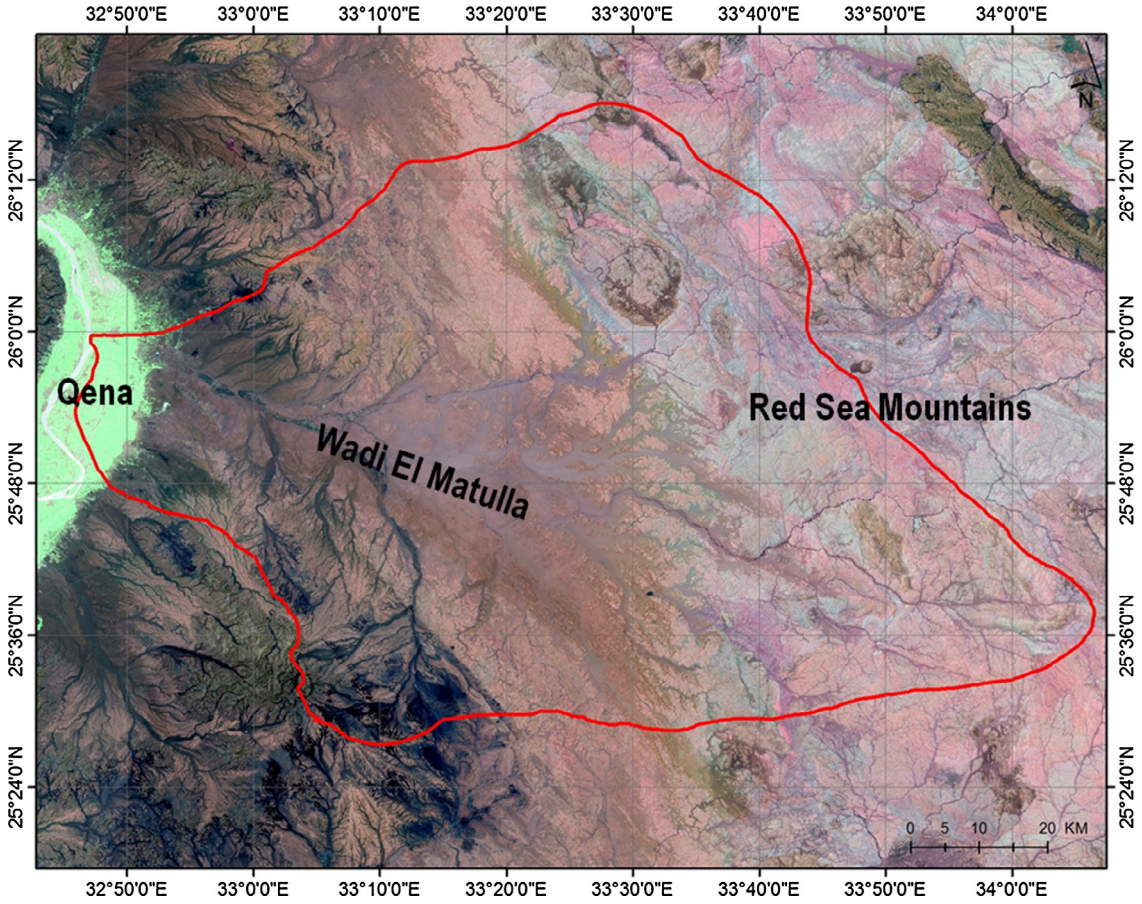


**Fig. 2.** Landsat-8 image of the Wadi El Matulla, East Qena City, and the red polygon shows the entire watershed surrounding the wadi.

Please cite this article in press as: Gaber, A., et al. Investigating the use of the dual-polarized and large incident angle of SAR data for mapping the fluvial and aeolian deposits. NRIAG Journal of Astronomy and Geophysics (2017), https://doi.org/10.1016/j.nrjag.2017.10.005

radar backscattered returns as a challenge to improve the contrast between the different targets and image the near-surface feature that might be hidden under the sand sheet.

## 3. Materials and methods

### 3.1. Characteristics of the used satellite dataset

In the first case study, Images from Landsat-8 and ALOS/PALSAR-1, which cover Wadi El Matulla, East Qena were used. The reflectance thermals bands of Landsat-8 indicated by path/row: 174/042 that acquired on February, 2nd, 2014 were used. In addition, four SAR dataset of ALOS/PALSAR-1 scenes (IDs: ALPSRP246050500, ALPSRP246050510, ALPSRP256990500 and ALPSRP256990510) were used with dual polarization (HH & HV), ascending orbit, product level 1.1, acquired on 6-September and 20-November 2010, with a right pointing antenna with range spacing 9.4 m and azimuth spacing 3.2 m and calibration factor −83 dB and incident angle ranging from 36.5° (near-range) and 40.1° (far-range). In addition visual assistant from Google Earth was carried out in order to evaluate the classification accuracy.

In this second case study, two adjacent and overlapped Radarsat-1 C-band images acquired in July 31st and August 7th, 2000 were used. These images were acquired in descending mode, HH polarization, right looking direction, 12.5 m pixel size, one look count, WD2 mode, 16 bits integer and with slant range to first pixel around 903649.4 m and incident angle ranging from 30.4° (near-range) and 39.8° (far-range). In addition, three full-polarimetric ALOS-PALSAR-1 L-band images acquired in April 8th, 2009, orbit/frames (17078/590, 17078/600 and 17078/610) were ordered. The acquisition characteristics of these images are in ascending mode, right looking, 7 look count, slant to first pixel around 750483.1 m, pixel size 9.4 m in range-direction and 3.5 m in azimuth-direction and incident angle ranging from 22.7° (near-range) and 25° (far-range).

For the optical data, the Landsat-7 and -8 images were used. The images of the years; Dec. 11, 1999, Feb. 22, 2000 of landsat-7 and Nov. 24, 2016 of landsat-8 with 30 m spatial resolution indicated by path/row (176/093 and 175/039) were downloaded from the public domain (http://earthexplorer.usgs.gov). However, in order to automatically extract the surface running drainage patterns and their watersheds along the study area in this second case study, the Shuttle Radar Topographic Mission (SRTM) dataset was used. In addition to the space-borne data, the geological, geomorphological and topographical maps of Sinai Peninsula were also used, geocoded and stored in a GIS database to prepare these layers for subsequent surface and subsurface correlation analysis.

### 3.2. Remote sensing data processing

#### 3.2.1. First case study

In this case study, an integrated use of the free software; polarimetric SAR Data Processing and Educational Toolbox (PolSARPro) and NEST together with the commercial software; ENVI-5.1 and ArcGIS were used to process the dual-polarimetric (HH and HV) PALSAR data. Each PALSAR image was individually imported to the PolSARPro software and then multilooked process was applied using one time in range and five times in azimuth direction. Subsequently, speckle noise was reduced by applying a $7 \times 7$ Lee-refined filter, followed by conversions to the $2 \times 2$ covariance matrix ($[C_2]$). Such $[C_2]$ matrix was used for deriving the polarimetric information and H/A/Alpha Decomposition (Cloude and Pottier, 1997) to investigate the radar scattering response of the different rock units, which cover the wadi deposits along the study area for accurately discriminating between them.

The obtained $[C_2]$ matrix as well as the three layers of the entropy (H), anisotropy (A) and alpha angel ($\alpha°$) were ingested in NEST software to geocode all these layers using map projection information as WGS84, UTM zone 36N and finally mosaic the 4 scenes of each layer and export them into a common GeoTiff format. The geocoded and mosaicked $[C_2]$ matrix was used in ENVI to stack its 4 components and generate a supervised classification map using predefined training sites derived from the, geologic map, field and Google Earth. In addition, the mean and standard deviation of the entropy, anisotropy and alpha values of each class of the generated supervised classification map were calculated in order to examine the dominant and the secondary radar scattering mechanism. This definitely helps to accurately differentiate between the obtained three classes (gravel, gravel/sand and sand). Aforementioned estimation has been done using the zonal statistics as table of the ArcGIS software, which spatially correlates two different layers and extracts information about each class from the other one.

Finally the reflectance bands (0.443–2.201 μm) and thermals bands (10.9–12 μm) of Landsat-8 were used in ENVI to calculate the average reflectance curve and land surface temperature curve of each class that was obtained from the aforementioned processing steps by automatically calibrating the multispectral bands into the top of atmosphere reflectivity and the thermal bands into brightness temperature using ENVI-5.1 software.

#### 3.2.2. Second case study

The two Radarsat-1 images were filtered using refined Lee filter using $5 \times 5$ window sizes to reduce the speckle noise and keep the details of the images. Consequently, these filtered Radarsat-1 images were automatically geocoded using the MapReady free software and exported into Geotiff format to be ingested in ArcGIS software. The others three full-polarimetric ALOS/PALSAR-1 images were converted from slant-range into ground-range resolution by applying the multiloock process using 7 looks in azimuth direction and 1 look in range direction. Then, these multilooked PALSAR data were calibrated, filtered, geocoded and mosaicked to generated 4 different images corresponding to the 4 different polarizations (HH, HV, VH and VV). Finally, these different images were imported in a GIS database in order to spatially correlate all these datasets. A hidden meandering stream under the sand sheet of the northwestern part of Sinai was clearly observed in only one Radarsat-1 image. Thus an intensive comparison between the different radar images was carried out to understand the reasons (mainly the contribution of the local incident angle) of why such hidden stream has been revealed in only one radar image and does not appear in the others images. The optical images were used here for visual comparison, obtained visual information regarding the surface roughness and generate change detection map for understanding the changes that occurred along the study area and might hid the observed stream, especially this stream has been observed in the Radarsat-1 image that was acquired in 2000 and this research work was conducted in 2017. Thus the change detection process was performed using the band math algebra of ENVI software to know the amount of changes along the study area during these 17 years' time differences. This change detection map has contributed a lot to locate the prober areas with no changes for future field work confirmation.

In this study, the DEM works aims at finding out if there are any surface or near-surface drainage patterns that similar to the revealed meandering stream. Thus, the eight directions model (D8), which was first introduced by O'Callaghan and Mark (1984) was performed. The streams were defined using thresholds values of 500, 1000, 2000, 3000, 4000 and 5000 cells to obtain different stream density maps.

Please cite this article in press as: Gaber, A., et al. Investigating the use of the dual-polarized and large incident angle of SAR data for mapping the fluvial and aeolian deposits. NRIAG Journal of Astronomy and Geophysics (2017), https://doi.org/10.1016/j.nrjag.2017.10.005

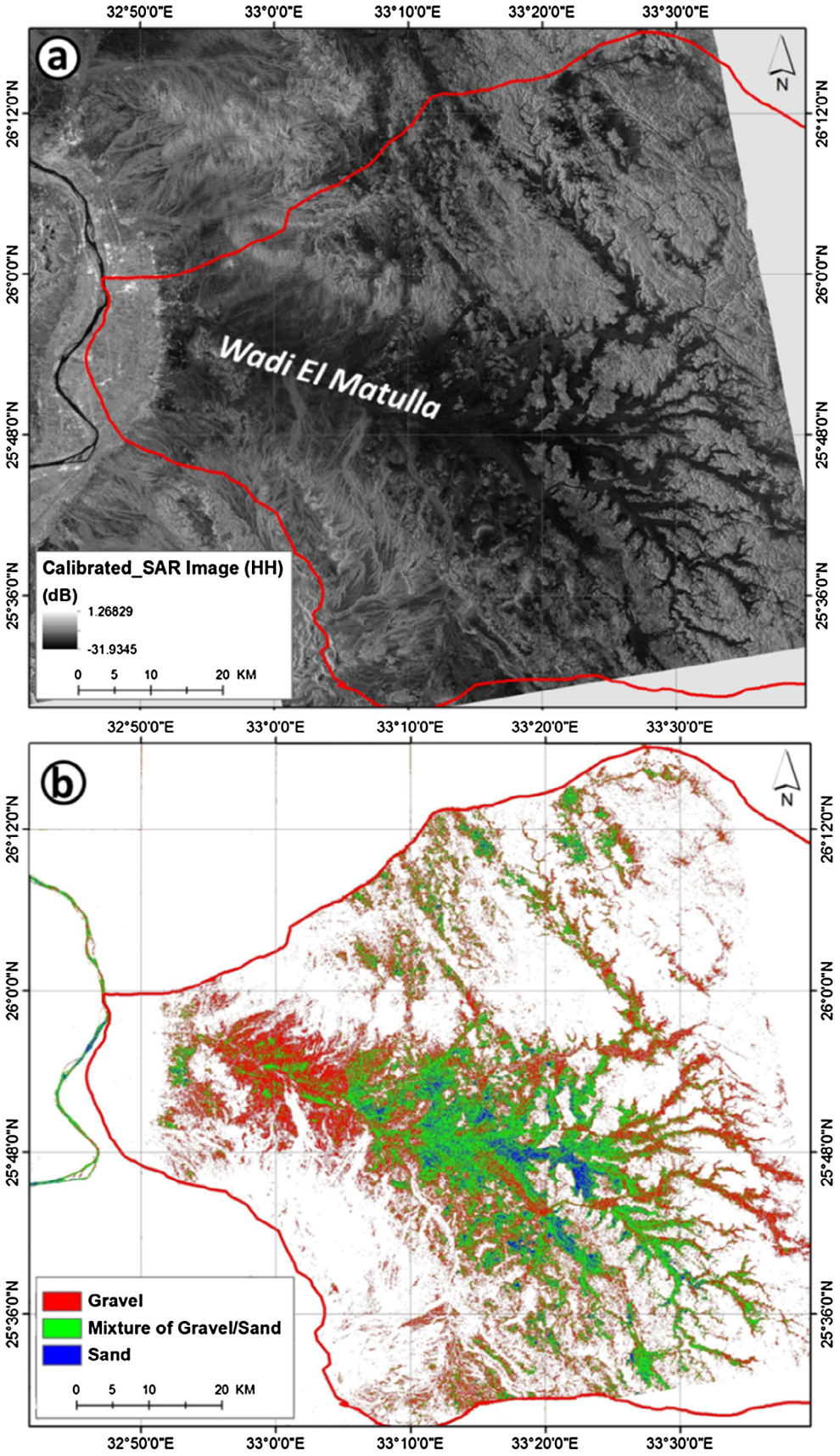


**Fig. 4.** The calibrated HH-PALSAR image (a) and the generated supervised classification map from the covariance matrix for the Wadi El-Mattula deposits (b).

Please cite this article in press as: Gaber, A., et al. Investigating the use of the dual-polarized and large incident angle of SAR data for mapping the fluvial and aeolian deposits. NRIAG Journal of Astronomy and Geophysics (2017), https://doi.org/10.1016/j.nrjag.2017.10.005

## 4. Results and discussions

### 4.1. First case study

The dual-polarized ALOS/PALSAR data provides an additional coherent HV channel allowing generating 2 × 2 covariance matrix ([$C_2$]). The supervised map of the wadis deposits was classified into three main classes (gravel, gravel/sand and sand) (Fig. 4b). The geologic map, landsat-8 and Google Earth together with the calculated radar backscatter coefficient ($\sigma^\circ$) map (Fig. 4a) were used to extract the reference points and generate this supervised classification map. The other land covers (e.g. vegetation, urban and water bodies) and different rock units were masked to show only the wadis deposits classes and its variations in terms of the degree of randomness of their radar scattering response which has a linear relationship with the grain sizes of the surface sediments.

In addition, the eigenvectors constructed from the [$C_2$] have been used to calculate the dual-polarimetric target parameters; entropy (H), anisotropy (A) and alpha angel ($\alpha^\circ$) by applying the

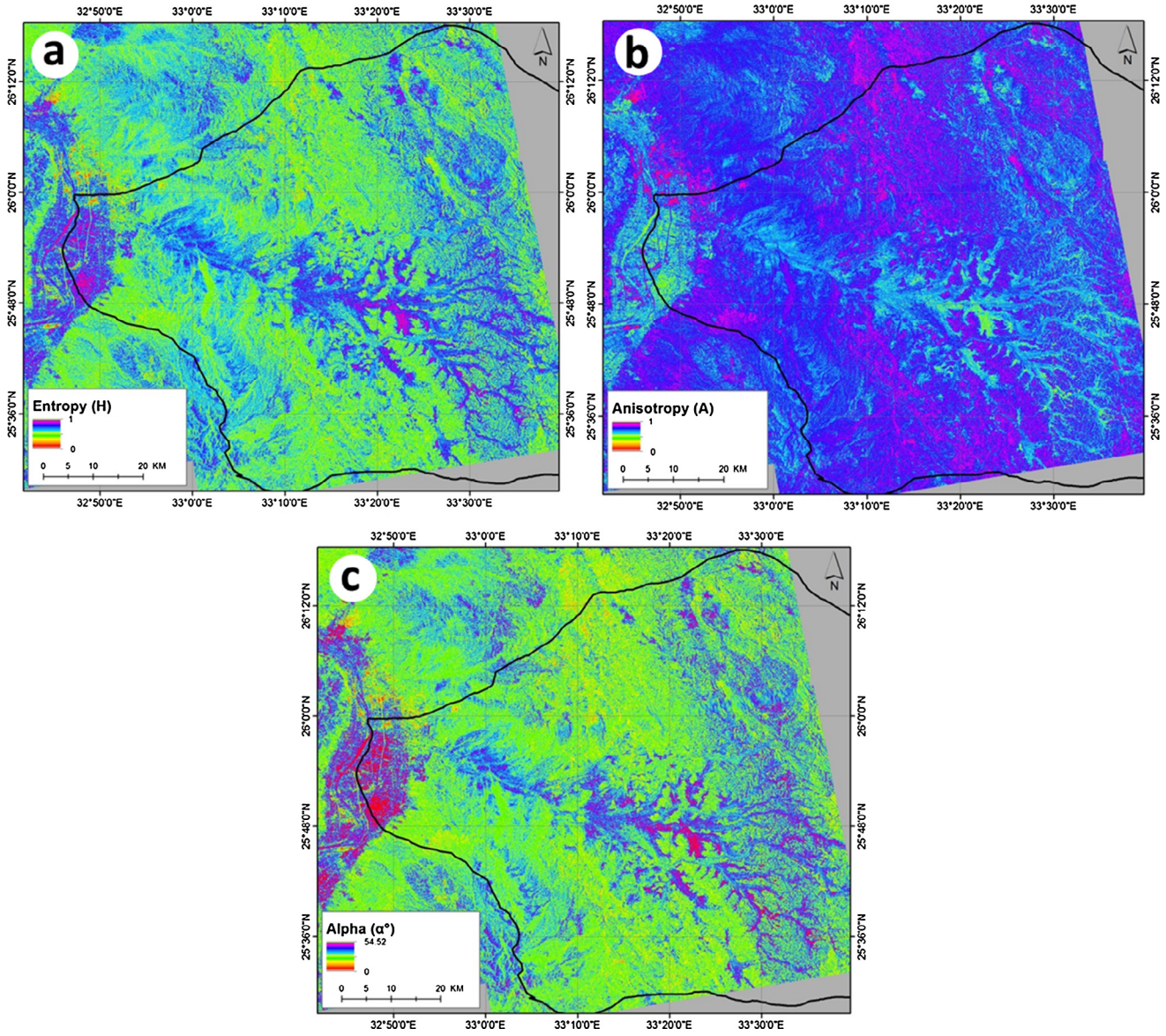


**Fig. 5.** The H/A/Alpha decomposition results, where entropy (a), anisotropy (b) and alpha angel (c) along the study area.

**Table 1**
The SAR scattering response of the Wadi El Matulla deposits.

| Sedimentary classes | SAR scattering mechanism | | | | | | Radar cross section ($\sigma^\circ$) | | | |
|---|---|---|---|---|---|---|---|---|---|---|
| | Alpha ($\alpha^\circ$) | | Entropy ($H$) | | Anisotropy ($A$) | | HH (dB) | | HV (dB) | |
| | Mean | STD. | Mean | STD. | Mean | STD. | Mean | STD. | Mean | STD. |
| Gravel | 22.13 | 3.59 | 0.72 | 0.07 | 0.73 | 0.06 | −20.57 | 0.93 | −28.46 | 1.53 |
| Gravel/Sand | 18.33 | 3.43 | 0.63 | 0.08 | 0.66 | 0.07 | −22.96 | 0.87 | −29.56 | 1.29 |
| Sand | 15.37 | 3.28 | 0.55 | 0.08 | 0.59 | 0.07 | −25.16 | 0.78 | −30.07 | 1.12 |

Please cite this article in press as: Gaber, A., et al. Investigating the use of the dual-polarized and large incident angle of SAR data for mapping the fluvial and aeolian deposits. NRIAG Journal of Astronomy and Geophysics (2017), https://doi.org/10.1016/j.nrjag.2017.10.005

H/A/Alpha Decomposition (Cloude and Pottier, 1997). Fig. 5 shows the H/A/Alpha decomposition results of the study area. In addition, the obtained results have been represented in Table 1 after spatially correlates the supervised classification map (Fig. 4b) with the three layers of the H/A/Alpha decomposition (Fig. 5) as well as the two calibrated HH and HV PALSAR images (Fig. 4a) using the zonal statistics as table of the ArcGIS software.

The results show that the gravel class has mean values of radar backscatter coefficient ($\sigma^\circ$) of the HH and HV polarization as −20.57 dB and −28.47 dB, with standard deviation of 0.93 and 1.53 dB, respectively. In addition, the mean values of its entropy (H), anisotropy (A) and alpha angel ($\alpha^\circ$), are 0.72, 0.73 and 22.13 with standard deviation of 0.07, 0.06 and 3.59, respectively (Table 1). While, the gravel/sand mixture class has mean values of radar backscatter coefficient ($\sigma^\circ$) of the HH and HV polarization as −22.96 dB and −29.56 dB, with standard deviation of 0.87 and 1.29 dB, respectively. The mean values of its entropy (H), anisotropy (A) and alpha angel ($\alpha^\circ$) are 0.63, 0.66 and 18.33 with standard deviation of 0.08, 0.07 and 3.34, respectively (Table 1). The sand class has mean values of radar backscatter coefficient ($\sigma^\circ$) of the HH and HV polarization as −25.16 dB and −30.07 dB, with standard deviation of 0.78 and 1.12 dB, respectively. The mean values of its entropy (H), anisotropy (A) and alpha angel ($\alpha^\circ$) are 0.55, 0.59 and 15.37 with standard deviation of 0.08, 0.07 and 3.28, respectively (Table 1).

The results show that the radar backscatter coefficient ($\sigma^\circ$) values of the gravel, gravel/sand and sand classes are increasing respectively by increasing their grain size as well as the degrees of randomness of their backscattered radar return waves, which have been derived from the H/A/Alpha angle values. These show the advantages of the dual-polarized ALOS/PALSAR data to classify the surface sediments in terms of their grain sizes.

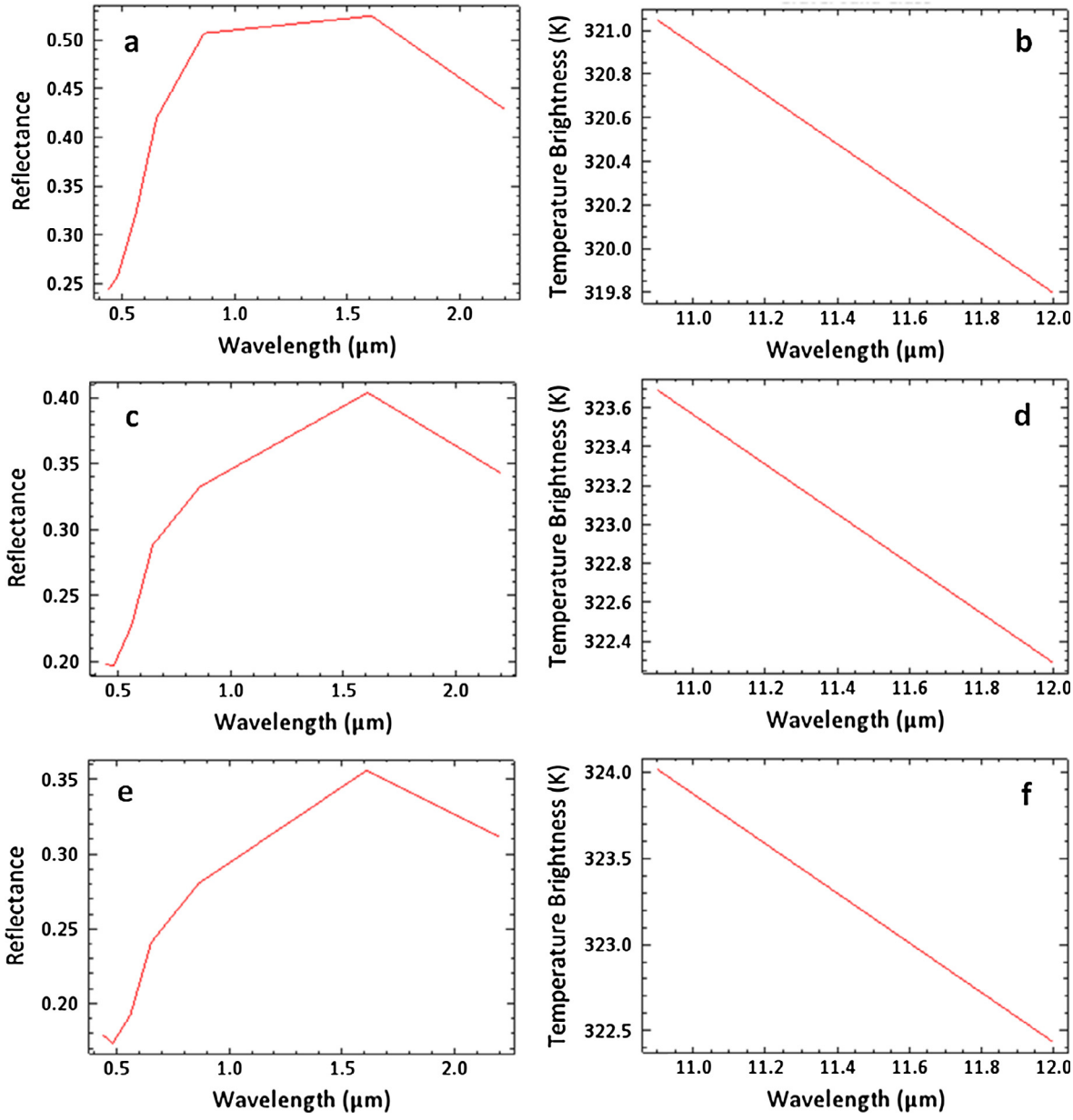


**Fig. 6.** (a, c and e) The average spectral reflectance curve of the gavel, gravel/sand and sand classes, respectively and (b, d and f) their corresponding temperatures brightness (K°).

Please cite this article in press as: Gaber, A., et al. Investigating the use of the dual-polarized and large incident angle of SAR data for mapping the fluvial and aeolian deposits. NRIAG Journal of Astronomy and Geophysics (2017), https://doi.org/10.1016/j.nrjag.2017.10.005

Moreover, the average spectral reflectance and the average temperature brightness of each class (gravel, gravel/sand and sand) were extracted from the calibrated visible and thermal bands of the optical Landsat-8 image (Fig. 6). The average normalized spectral reflectance of the gravel, gravel/sand and sand classes are around 0.53, 0.4 and 0.35, while their average temperatures brightness are around 321.1 K, 323.8 K and 324 K, respectively (Fig. 6).

The integrated results show that the gravel class has the higher random backscattering radar return, the higher average spectral reflectance and the lower average temperatures brightness, which means this class is the larger in terms of gran sizes, more brighter and less conductive (less heterogeneous) than the other two classes (gravel/sand and sand). While the sand class shows the opposite behavior to the gravel class, which means this class is the smaller in terms of grain size, and darker in color and more conductive (more heterogeneous) than the other two class. The gravel/sand mixture class is in between the others two classes. This confirms that the dual-polarized SAR data can help a lot in discriminating the surficial sediments in terms of surface roughness (grain size) and add information about their radar response.

### 4.2. Second case study

In very dry soils such desert environments, SAR sensors are able to probe the subsurface of low electrical loss material such as sand. In this study the large incident angle ($\theta_i = 39.7°$) of the Radarsat-1 image acquired in July 31st, 2000 has revealed a meandering buried river under the sand sheet of the northwestern part of Sinai (Fig. 7). In this case study, different optical, SRTM and SAR images for the same area and acquisition year with different wavelengths, incident angles and polarizations modes were used to compare and check if such buried paleoriver can be observed or not. None of the supported images show such hidden stream.

Fortunately, the right image of Fig. 7 is the only SAR image, where we can observe such hidden meandering stream, because such buried feature is located at the far-range of the Radarsat-1 image with large incident angle which improved a lot the radar backscattered return compared to the others SAR data and thus enhanced the contrast between the low backscattered targets and its surrounding. Whereas, the local incident angle ($\theta_i$) in the far-range usually has high backscattered intensity more than the

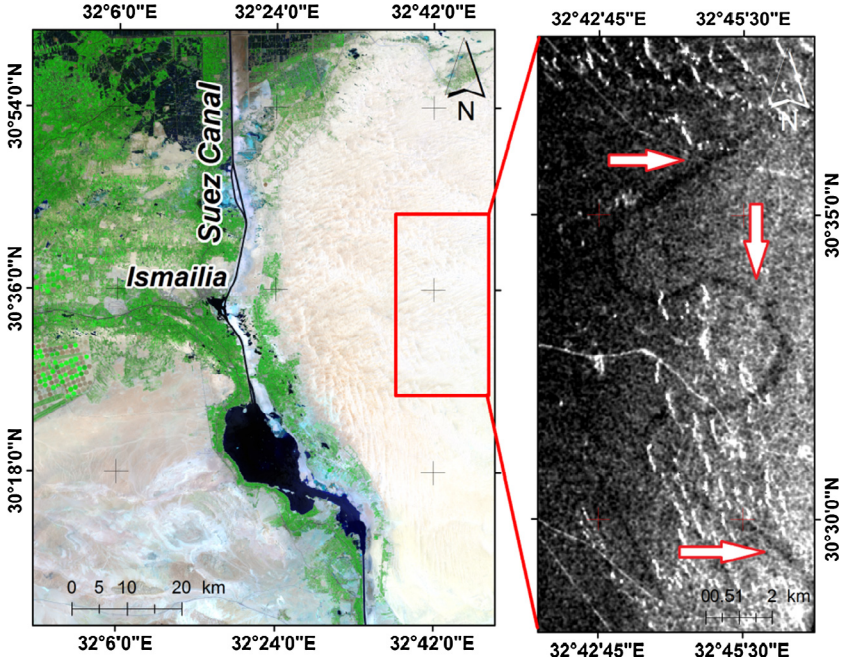


**Fig. 7.** The optical landsat-8 image of the study area (left) and the revealed meandering hidden stream using the Radarsat-1 image (right).

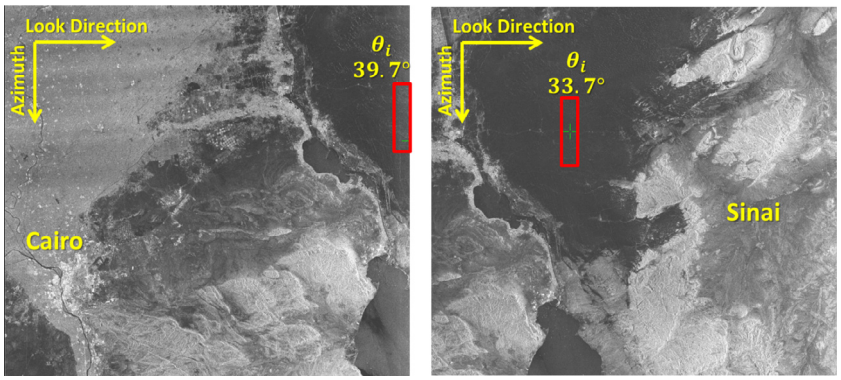


**Fig. 8.** The locations of the hidden meandering stream with red rectangular on both Radarsat-1 images. In the left image the hidden feature can be observed because it is located at the far-range with larger incident angle ($\theta_i = 39.7°$), while in the right image the feature cannot be observed because it is located almost in the middle of the image with smaller incident angle ($\theta_i = 33.7°$).

Please cite this article in press as: Gaber, A., et al. Investigating the use of the dual-polarized and large incident angle of SAR data for mapping the fluvial and aeolian deposits. NRIAG Journal of Astronomy and Geophysics (2017), https://doi.org/10.1016/j.nrjag.2017.10.005

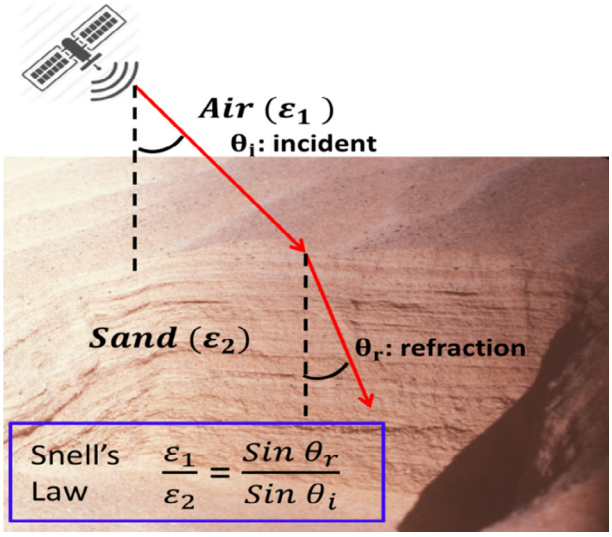


**Fig. 9.** Two layer sketch model of the incident and refracted angles with Snell's Law.

near-range one along the areas with the same surface roughness. The second Radarsat-1 image, which has been acquired only one week later does not show such hidden meandering stream because the observed feature is located at smaller local incident angle ($\theta_i$ = 33.7°) with 6° less (Fig. 8).

Based on Snell's Law and assuming the dielectric constant of the sand ($\varepsilon_2$) which covers the study area is higher than the dielectric constant of the air ($\varepsilon_1$), the penetration depth of the satellite ($\delta p'$) will controlled by the following equation (Gay and Ferro-Famil, 2016):

$$\delta p' = \delta p \cos_r \quad (4)$$

where $\delta p$ represents the maximum depth within a medium that can contribute to the backscattering coefficient and is the angle of refraction (Fig. 9). This means the small incident angle the small penetration depth of the satellite and the opposite is true. In this case study the hidden features appears in large incident angle, which means such observation does not relate to the penetration depth but more related to the increasing in the backscattered intensity of the returned radar signals. Moreover, the longer wavelength of the L-band ALOS/PALSAR with its different polarizations dose not image such hidden feature, because of its smaller incident angle, which is ranging from 22.7° (near-range) and 25° (far-range) and thus it produce a weak backscattered intensity.

Thus the main reason to image such hidden meandering stream is the high backscattering intensity of the radar returns which is related to the relatively higher incident angle along the rough surface and consequently enhances the contrast between the targets that have low backscattering response. The surface roughness along the study area is relatively undulated (rough) due to the existence of the sand dunes with different directions (Fig. 10b). The generated change detection map using the optical data acquired in 2000 and 2016 (Band 7-7) (Fig. 10c) can be used for future field work survey using the ground penetrating radar (GPR) along the areas where small changes have been occurred. In addition, the digital elevation model (DEM) of the SRTM was used to extract the drainage patterns along study area and compare it with the revealed hidden paleo-river and investigate if there are any surface streams running close or parallel to the observed buried one. The SRTM has been performed using the same C-band of Radarsat-1 sensor and should have some penetration capability in the desert sand areas. Different flow accumulation thresholds values were performed to get different streams density maps (Fig. 11).

The observations after extracting different drainage patterns density maps show that none of the extracted surface or near-surface drainage patterns are close in direction to the meandering

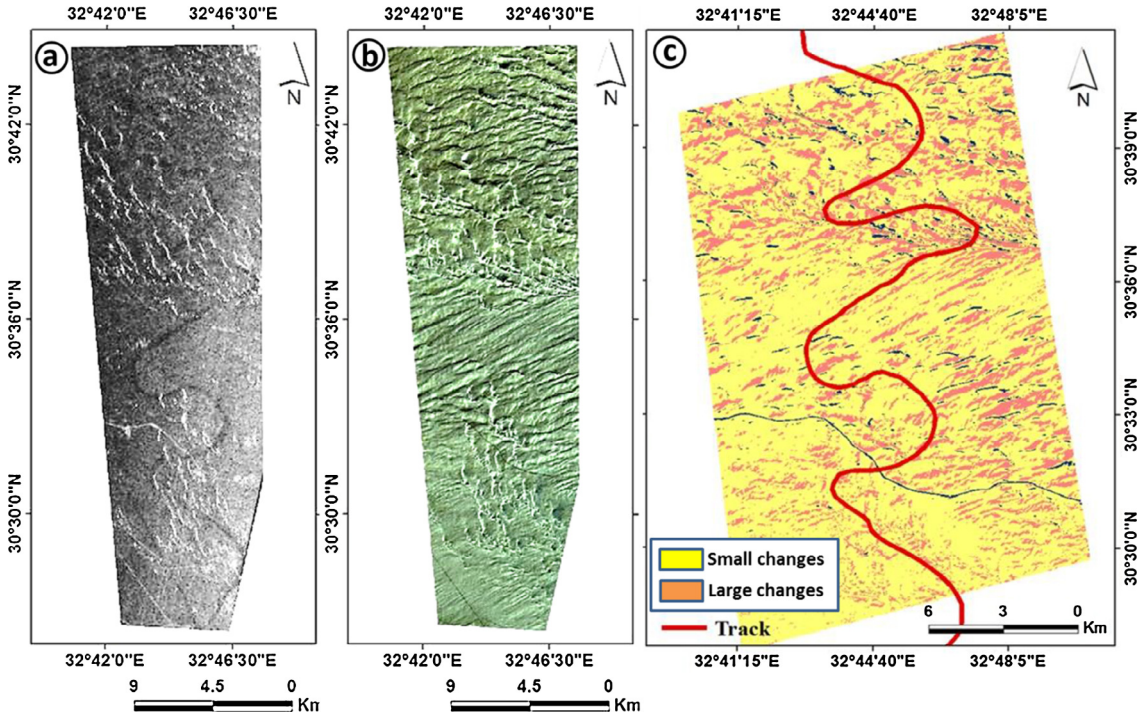


**Fig. 10.** The revealed meandering stream from Radarsat-1 image (a), the sand dunes which make the ground surface very rough and increased the radar backscattered intensity with the large local incident angle (b) and the optical generated change detection map (c).

Please cite this article in press as: Gaber, A., et al. Investigating the use of the dual-polarized and large incident angle of SAR data for mapping the fluvial and aeolian deposits. NRIAG Journal of Astronomy and Geophysics (2017), https://doi.org/10.1016/j.nrjag.2017.10.005

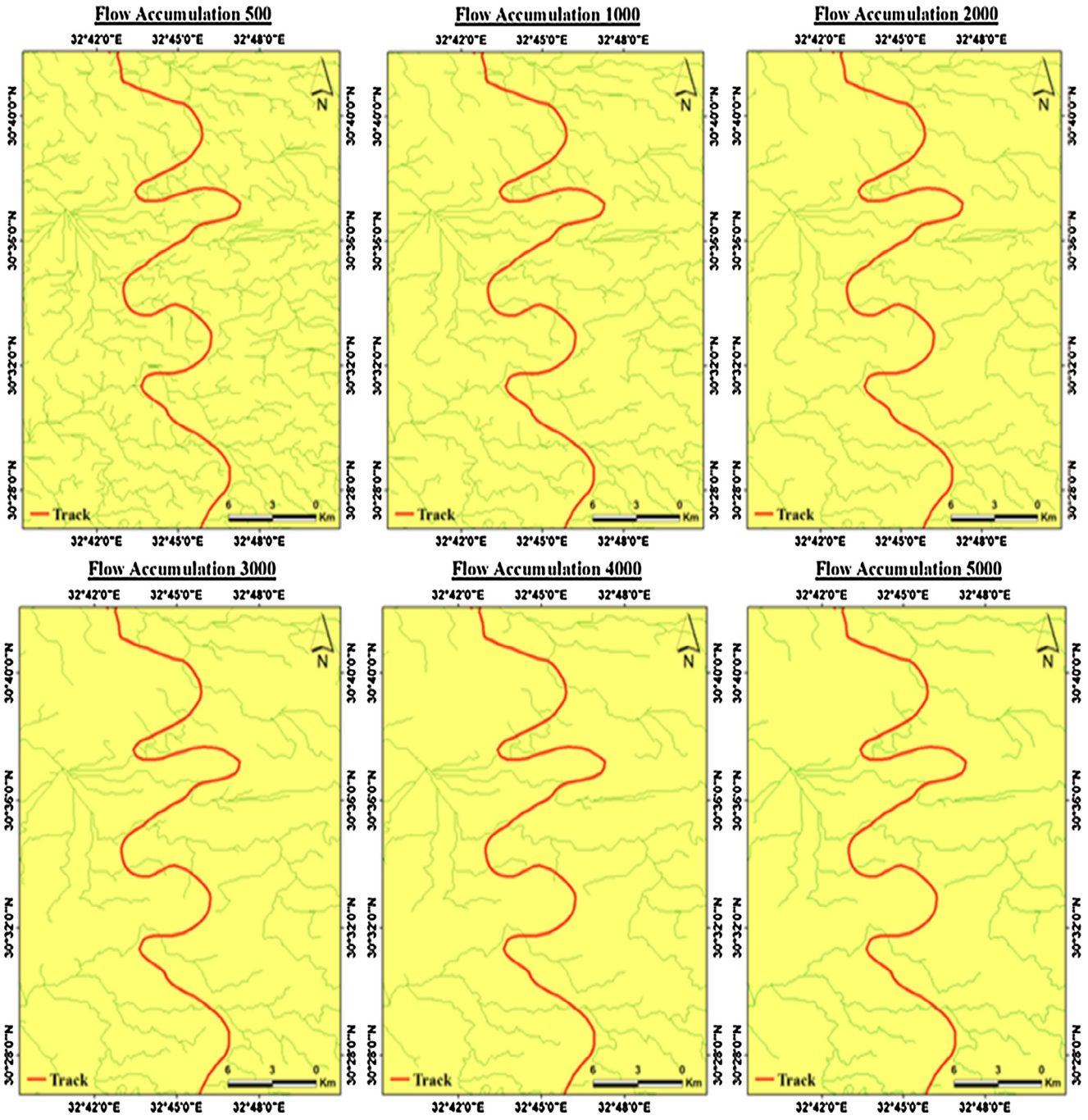


**Fig. 11.** The automatically generated drainage patterns using the SRTM with different flow accumulation threshold values (drainage densities) and the track of the revealed stream is plotted by red line. (For interpretation of the references to color in this figure legend, the reader is referred to the web version of this article.)

stream that has been revealed using the far-range and high incident angle of Radarsat-1 image. The automatically generated drainage patterns using the SRTM data are mostly have NW-SE directions, and according to the published structural maps (Sayed, 2016), the study area is surrounded by faults and lineation regime with the same NW-SE directions that might be related to the Oligocene age (Gulf of Suez). These NW-SE faults trends support that the surface water is running toward the same direction and controlled by the topographic surface criteria, which were affected by the subsurface structures. Therefore, the sediment load of the current and past fluvial channels would have been deposited in low-relief areas along its way. As the climate became drier, these sediments have been exposed to the action of the wind. The latter mobilized and sculptured the sand into various dune forms, depending on the amount of available sand and the prevailing wind directions. On the other hand, the paleo-environmental and archeological studies, which have been performed along the study area, confirmed the existence of ancient fresh-water streams and marshy swamps (Hoffmeier and Moshier, 2006). All these archaeological observations support the existence of paleo-fresh water lagoon at the northwest corner of the study area, which might be was the discharge lagoon of the revealed hidden stream (Fig. 12).

Please cite this article in press as: Gaber, A., et al. Investigating the use of the dual-polarized and large incident angle of SAR data for mapping the fluvial and aeolian deposits. NRIAG Journal of Astronomy and Geophysics (2017), https://doi.org/10.1016/j.nrjag.2017.10.005

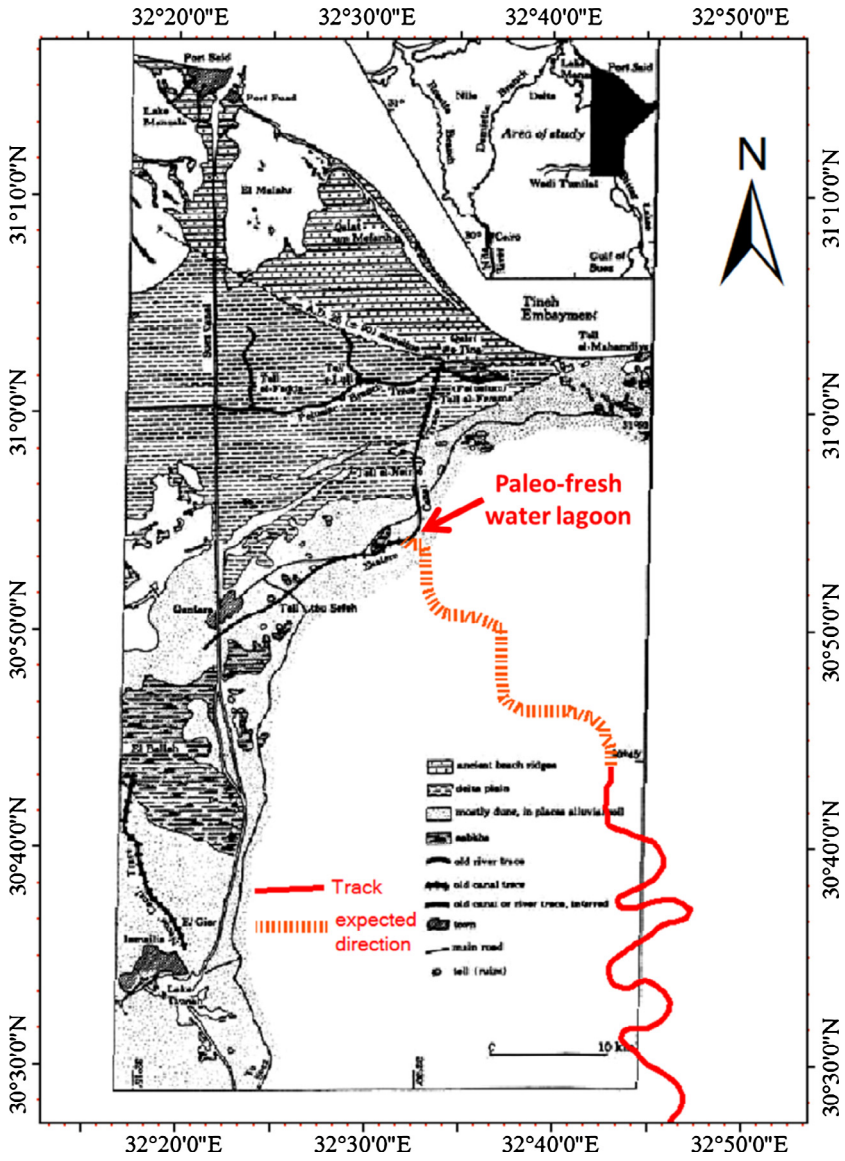


**Fig. 12.** Paleo-environmental map of the northeastern delta (modified after Hoffmeier and Moshier, 2006). The track of the revealed stream is plotted by the solid red line, while the dashed red line is the proposed direction toward the paleo-fresh-water lagoon. (For interpretation of the references to color in this figure legend, the reader is referred to the web version of this article.)

## 5. Conclusion

The polarimetric information of SAR data provides valuable input for discriminating and classifying the surface sediments and land covers. Since, the dual-polarized ALOS/PALSAR data allows generating the covariance matrix ($[C_2]$), the eigenvectors constructed and have been used in East Qena (1st case study) to calculate the dual-polarimetric target parameters; entropy (H), anisotropy (A) and alpha angel ($\alpha^\circ$) by applying the H/A/Alpha decomposition. Moreover, such matrix has been stacked and used to generate a supervised classification map for the wadis deposits along the Wadi El-Matulla, East Qena, Egypt. The surface sediments have been classified into 3 classes (gravel, gravel/sand and sand). The scattering response, radar backscattering coefficients, average spectral reflectance and average thermal brightness of each class have been calculated, which have significant contribution in mapping the surface fluvial sediments accurately.

Moreover, the large local incident angles of SAR data will obviously improve the backscattering intensity of the returned radar signals along a relatively rough surface and consequently enhanced the contrast between the targets that have low backscattered return and the surroundings. This proven theoretical fact has been introduced in this study using a real example in an undulated sandy aeolian area of the northwestern part of Sinai Peninsula, Egypt (2nd case study). For this purpose, several SAR datasets with different incident angles, wavelengths and polarizations were processed and used. Out of this set of SAR data, only one Radarsat-1 image with the highest incident angle ($\theta_i = 38.7^\circ$) revealed a hidden meandering stream at its far-range and thus improved a lot the radar backscattered return compared to the others SAR data. The paleo-environmental and archeological studies which have been performed along this study area confirmed the existence of ancient fresh-water streams and marshy swamps. All these archaeological observations support the existence of paleo-fresh water lagoon at the northwest corner of the study area, which might be the discharge lagoon of the revealed hidden stream. A field confirmation visit will be carried out in the near-future to perform ground penetrating radar (GPR) survey to validate the existence of such revealed stream after issuing the required security permissions, since the study area is unsecure now.

Please cite this article in press as: Gaber, A., et al. Investigating the use of the dual-polarized and large incident angle of SAR data for mapping the fluvial and aeolian deposits. NRIAG Journal of Astronomy and Geophysics (2017), https://doi.org/10.1016/j.nrjag.2017.10.005

## Acknowledgements

The authors would like to thank the Center for Remote Sensing, Boston University, USA for providing the Radarsat-1 images. In addition, the authors would like to thank JAXA for providing the full-polarimetric ALSO/PALSAR-1 data as part of the ALOS user agreement (ALOS-2 RA-1389) as well as Dr. Said Nawar from Suez Canal University for providing the dual-polarized ALOS/PALSAR-1 data. Further thanks are given to Dr. Magaly Koch from Boston University for her valuable discussion and comments. The authors are thankful for the help made by Ismail from Suez Valley University and Ayman and Hossam from Port-Said University. Finally, the authors are very grateful for the very helpful suggestions made by the reviewers.

## References

Abdelsalam, M.G., Robinson, C., El-Baz, F., Stern, R.J., 2000. Applications of orbital imaging radar for geologic studies in arid regions: the Saharan testimony. Photogram. Eng. Remote Sens. 66, 717–726.

Al Hussein, A., Basheer, Osman, Salah, S., Tahal, Ayman I., 2012. Assessment of the saline water intrusion through the fresh groundwater aquifer by using ER and TEM methods at the Qantara Shark Area, Sinai, Egypt. Int. J. Innov. Res. Dev. 3 (4), 398–406.

Alberga, V., 2007. A study of land covers classification using polarimetric SAR parameters. Int. J. Remote Sens. 28 (17), 3851–3870.

Barnes, C.F., Burki, J., 2006. Late-season rural land-cover estimation with polarimetric-SAR intensity pixel blocks and sigma-tree-structured near-neighbor classifiers. IEEE Trans. Geosci. Remote Sens. 44 (9), 2384–2392.

Cameron, W.L., Rais, H., 2006. Conservative polarimetric scatterers and their role in incorrect extensions of the Cameron decomposition. IEEE Trans. Geosci. Remote Sens. 44 (12), 3506–3516.

Chen, K.S., Huang, W.P., Tsay, D.H., Amar, F., 1996. Classification of multifrequency polarimetric SAR imagery using a dynamic learning neural network. IEEE Trans. Geosci. Remote Sens. 34 (3), 814–820.

Cloude, S.R., Pottier, E., 1996. A review of target decomposition theorems in radar polarimetry. IIEEE Trans. Geosci. Remote Sens. 34 (2), 498–518.

Cloude, S.R., Pottier, E., 1997. An entropy based classification scheme for land applications of polarimetric SAR. IEEE Trans. Geosci. Remote Sens. 35 (1), 68–78.

Lusch, David P., 1999. In: Introduction to Microwave Remote Sensing" Basic Science and Remote Sensing Intiative. Department of Geography, Michigan State University, p. 84.

EGSM, 1987. Geological Map of Eastern Desert, Egypt. Scale 1: 500 000. The Egyptian General Petroleum Corporation, Cairo, Egypt.

Elachi, C., Roth, L.E., Schaber, G.G., 1984. Spaceborne radar subsurface imaging in hyper-arid regions. IEEE Trans. Geosci. Remote Sens. 22, 383–388.

El-Baz, F. Robinson, C., Al-Saud. T., 2007. Radar images and geomorphology of the eastern Sahara. In: Wiseman, J., El-Baz, F. (Eds.). Remote Sensing in Archaeology. Springer, New York, pp. 1–8.

Farr, T.G., Elachi, C., Hartl, P., Chowdhury, K., 1986. Microwave penetration and attenuation in desert soil: a field experiment with the Shuttle Imaging Radar. IEEE Trans. Geosci. Remote Sens. GE-24, 590–594.

Ferro-Famil, L., Pottier, E., Lee, J.S., 2001. Unsupervised classification of multifrequency and fully polarimetric SAR images based on the H/A/Alpha-Wishart classifier. IEEE Trans. Geosci. Remote Sens. 39 (11), 2332–2342.

Freeman, A., Durden, S.L., 1998. A three-component scattering model for polarimetric SAR data. IEEE Trans. Geosci. Remote Sens. 36 (3), 963–973.

Gaber, A., Soliman, F., Koch, M., El-Baz, F., 2015. Using full-polarimetric SAR data to characterize the surface sediments in desert areas: A case study in El-Gallaba Plain, Egypt. Remote Sens. Environ. 162, 11–28.

Gay, M., Ferro-Famil, L., 2016. Penetration depth of Synthetic Aperture Radar signals in ice and snow: an analytical approach. Workshop Remote Sensing and Modeling of Surface Properties. p. 23.

Ghasemi, A., Abedi, A., Ghasemi, F., 2016. Propagation Engineering in Wireless Communications. Springer Publishing. doi: 10.1007/978-1-4614-1077-52 p. 448.

Ghoneim, E., Robinson, C., El-Baz, F., 2007. Radar topography data reveal drainage relics in the eastern Sahara. Int. J. Remote Sens. 28 (8), 1759–1772.

Hoffmeier, James K., Moshier, S., 2006. New paleo-environmental evidence from North Sinai to complement manfred Bietak's map of the eastern delta and some historical implications. In: Czerny, E., Hein, I., Hunger, H., Melman, D., Schwab, A. (Eds.). Timelines: Studies in Honour of Manfred Bietak, vol. II, pp. 167–176.

Lee, J.S., Grunes, M.R., Ainsworth, T.L., Du, L.J., Schuler, D.L., Cloude, S.R., 1999. Unsupervised classification using polarimetric decomposition and the complex Wishart classifier. IEEE Trans. Geosci. Remote Sens. 37 (5), 2249–2258.

McCauley, J.F., Schaber, G.G., Breed, C.S., Grolier, M.J., Haynes, C.V., Issawi, B., et al., 1982. Subsurface valleys and geoarchaelology of Egypt and Sudan revealed by radar. Science 218, 1004–1020.

Mouginis, P., 2017. Introduction to Radar Remote Sensing. <http://satftp.soest.hawaii.edu/space/hawaii/vfts/kilauea/radar_ex/page2.html>.

O'Grady, D., Leblanc, M., Gillieson, D., 2013. Relationship of local incidence angle with satellite radar backscatter for different surface conditions. Int. J. Appl. Earth Observ. Geoinf. 24, 42–53.

O'Callaghan, J.F., Mark, D.M., 1984. The extraction of drainage networks from digital elevation data. Comput. Vision Graph. Image Process. 28 (3), 323–344.

Paillou, P., 2017. Mapping palaeohydrography in deserts: contribution from space-borne imaging radar. Water 9, 194. https://doi.org/10.3390/w9030194.

Paillou, P., Grandjean, G., Baghdadi, N., Heggy, E., August-Bernex, T., Achache, J., 2003. Subsurface imaging in south-central Egypt using low-frequency radar: Bir Safsaf revisited. IEEE Trans. Geosci. Remote Sens. 41, 1672–1684.

Paillou, P., Reynard, B., Malézieux, J.-M., Dejax, J., Heggy, E., Rochette, P., Reimold, W. U., Michel, P., Baratoux, D., Razin, P., et al., 2006. An extended field of crater-shaped structures in the Gilf Kebir region—Egypt: observations and hypotheses about their origin. J. Afr. Earth Sci. 46, 281–299.

Paillou, P., Schuster, M., Tooth, S., Farr, T., Rosenqvist, A., Lopez, S., Malézieux, J.-M., 2009. Mapping of a major paleodrainage system in Eastern Libya using orbital imaging Radar: the Kufrah River. Earth Planet. Sci. Lett. 277, 327–333.

Paillou, P., Lopez, S., Farr, T., Rosenqvist, A., 2010. Mapping subsurface geology in Sahara using L-band SAR: First Results from the ALOS/PALSAR imaging radar. IEEE J. Select. Top. Earth Obs. Remote Sens. 3, 632–636.

Papathanassiou, K.P., Buchroithner, M.F., 1993. Signature analysis of multifrequency polarimetric NASA DC-8 Airsar data of alpine geo-applications. EARSeL Adv. Remote Sens. 2 (1-I), 287–299.

Rignot, E., Chellappa, R., Dubois, P., 1992. Unsupervised segmentation of polarimetric SAR data using the covariance matrix. IEEE Trans. Geosci. Remote Sens. 30 (4), 697–705.

Robinson, C., El-Baz, F., Ozdogan, M., Ledwith, M., Blanco, D., Oakley, S., Inzana, J., 2000. Use of radar data to delineate palaeodrainage flow direction in the Selima sand sheet, Eastern Sahara. Photogram. Eng. Remote Sens. 66, 745–753.

Sayed, I. Selim, 2016. The integration of gravity, magnetic and seismic data in delineating the sedimentary basins of northern Sinai and deducing their structural controls. J. Asian Earth Sci. 115, 345–367.

Schaber, G.G., McCauley, J.F., Breed, C.S., 1987. The use of multifrequency and polarimetric SIR-C/X-SAR data in geologic studies of Bir Safsat, Egypt. Remote Sens. Environ. 59, 337–363.

Schaber, G.G., McCauley, J.F., Breed, C.S., Olhoeft, G.R., 1986. Shuttle imaging radar: physical controls on signal penetration and subsurface scattering in the eastern Sahara. IEEE Trans. Geosci. Remote Sens. GE-24 (4), 603–623.

Ulaby, F.T., Moore, R.K., Fung, A.K., 1982. In: Microwave Remote Sensing; Active and Passive: V.2, Radar Remote Sensing and Surface Scattering and Emission Theory. Reading Addison-Wesley, pp. 457–1064.

Van Zyl, J.J., 1989. Unsupervised classification of scattering behavior using radar polarimetry data. IEEE Trans. Geosci. Remote Sens., 36–45

Van Zyl, J.J., Zebker, H.A., Elachi, C., 1987. Imaging radar polarization signatures: theory and observation. Radio Sci. 22, 529–543.

Yamaguchi, Y., Moriyama, T., Ishido, M., Yamada, H., 2005. Four-component scattering model for polarimetric SAR image decomposition. IEEE Trans. Geosci. Remote Sens. 43 (8), 1699–1706.

Yang, J., Yamaguchi, Y., Yamada, H., Sengoku, M., Lin, S.M., 1998. Stable decomposition of mueller matrix. IEICE Trans. Commun. E81-B (6), 1261–1268.

Zhang, Fengli, Xu, Maosong, Xie, Chou, Xia, Zhongsheng, Li, Kun, AiminCai, Yun Shao, Wang, Xuejun, Touzi, Ridha, 2011. Polarimetric signature and the temporal variation analysis for deforestation mapping in Southwest China. PIERS 7 (7), 613–616.

Please cite this article in press as: Gaber, A., et al. Investigating the use of the dual-polarized and large incident angle of SAR data for mapping the fluvial and aeolian deposits. NRIAG Journal of Astronomy and Geophysics (2017), https://doi.org/10.1016/j.nrjag.2017.10.005